U.S. Department of Transportation
Federal Aviation Administration

FINAL PROJECT REPORT

Form Approved:
O.M.B. No. 2120-0559
9/30/2013

PART I - PROJECT IDENTIFICATION INFORMATION

1. Institution and Address	2. FAA Program	3. FAA Award Number
Purdue University, West Lafayette, Indiana, USA	ASCENT: NJFCP	COE-2014-29A, 401321
	4. Award Period From 11/5/14 To 12/19/20	5. Cumulative Award Amount $1,020,000

6. Project Title

Project 029(A) National Jet Fuels Combustion Program – Area #5: Atomization Test and Models

PART II - SUMMARY OF COMPLETED PROJECT (For Public Use)

The objectives of this project, as stated in the Invitation for ASCENT COE Notice of Intent (COE-2014-29), are to "measure the spray characteristics of the nozzles used in the Referee Combustor used in Area 6 tests and to develop models for characterizing the atomization and vaporization of the reference fuels." We conducted experiments within the joint experimental and modeling effort. The experimental tasks were performed at Purdue University, and the modeling tasks were performed by Prof. Matthias Ihme's group at Stanford University, Prof. Suresh Menon's group at Georgia Tech, and Vaidya Sankaran's group at United Technologies Research Center (UTRC). Nader Rizk developed spray correlations based on the measurements.

Purdue University has highly capable test facilities for measuring spray characteristics over wide ranges of pressure, air temperature, and fuel temperature. The experimental diagnostics applied in this project included PDA and high-frame-rate shadowgraphy. The atomization and spray dynamics for multiple reference and candidate alternative fuels were characterized for the referee rig nozzle operating under near-LBO conditions. The referee rig operation was modeled using novel large-eddy simulation techniques featuring adaptive mesh refinement.

PART III - TECHNICAL INFORMATION (For Program Management Uses)

1. **ITEM** (Check appropriate blocks)	NONE	ATTACHED	PREVIOUSLY FURNISHED	TO BE FURNISHED SEPARATELY TO PROGRAM	
				Check (X)	Approx. Date
a. Abstracts of Theses			X		
b. Publication Citations			✘		
c. Data on Scientific Collaborators			✘		
d. Information on Inventions	✘				
e. Technical Description of Project and Results			✘		
f. Other (specify)					

2. Principal Investigator/Project Director Name (Typed)	3. Principal Investigator / Project Director Signature	4. Date
Robert P. Lucht	Robert P. Lucht	11/9/2021

FAA Form 9550-5 (03-03) Supersedes Previous Edition

INSTRUCTIONS FOR FINAL PROJECT REPORT

One copy of this report is due within 90 days after the expiration of the award. It should be submitted to the cognizant technical monitor in the FAA award letter.

INSTRUCTIONS FOR PART I

These identifying data items should be the same as on the award documents.

INSTRUCTIONS FOR PART II

The summary (about 200 words) must be self-contained and intelligible to a scientifically literate reader. Without restating the project title, it should begin with a topic sentence stating the project's major thesis. The summary should include, if pertinent to the project being described, the following items:

- The primary objectives and scope of the project. The techniques or approaches used
- (only to the degree necessary for comprehension). The findings and implications
- stated as concisely and informatively as possible.

FAA may disseminate the project report through the National Technical Information Service (NTIS) of the Department of Commerce. Authors should also be aware that the summary may be used to answer inquiries by nonscientists as to the nature and significance of the supported activity. Scientific jargon and abbreviations should be avoided.

INSTRUCTIONS FOR PART III

Items in Part III may, but need not, be submitted with this Final Project Report. Place a check mark in the appropriate block next to each item to indicate the status of your submission.

a. Self-explanatory.

b. For publications (published and planned) include title, journal or other reference, date, and authors. Provide two copies of any reprints as they become available.

c. Scientific Collaborators provide a list of co-investigators, research assistants and others associated with the project. Include title or status, e.g. associate professor, graduate student, etc.

d. Briefly describe any inventions which resulted from the project and the status of pending patent applications, if any.

e. Provide a technical summary of the activities and results. The information supplied in proposals for further support, updated as necessary, may be used to fulfill this requirement.

f. Include any additional material, either specifically required in the award instrument (e.g. special technical reports or products such as films, books, studies) or which are considered to be useful to the Foundation.

PAPERWORK REDUCTION ACT

Project 029(A) National Jet Fuel Combustion Program – Area #5: Atomization Test and Models Final Report

Purdue University

Project Lead Investigator

Robert P. Lucht
Ralph and Bettye Bailey Distinguished Professor of Combustion
School of Mechanical Engineering
Purdue University
West Lafayette, IN 47907-2088
Cell: 765-714-6020
Lucht@purdue.edu

University Participants

Purdue University

- PIs: Robert P. Lucht, Jay P. Gore, Paul E. Sojka, and Scott E. Meyer
- FAA Award Number: 13-C-AJFE-PU, Amendments: 05, 11,16, 21, 28, 30
- Period of Performance: December 1, 2014 to December 19, 2020
- Tasks:
    1. Obtain phase Doppler anemometry (PDA), Mie scattering, and fuel laser-induced fluorescence data in the variable ambient pressure spray (VAPS) test rig operated with the referee rig nozzle for numerous fuels under near-lean blowout (near-LBO) conditions and under cold fuel/cold air flow conditions approximating ground light-off (GLO) and high-altitude relight conditions (HAR).
    2. Perform computational fluid dynamics (CFD) simulations of the referee rig under near-LBO and LBO conditions for different fuels.

Project Funding Level

The funding level from FAA was $1,020,000 to Purdue University. Purdue University provided cost-sharing funds.

Investigation Team

- PI Dr. Robert Lucht, Bailey Distinguished Professor of Mechanical Engineering, is responsible for overseeing the project at Purdue University. He is also responsible for mentoring one of the graduate students, coordinating activities with Stanford, working with all parties for appropriate results, and reporting results as required.
- Co-PI Dr. Jay P. Gore, Reilly Professor of Mechanical Engineering, works closely with the PI and oversees the work performed by one of the graduate students. He is also responsible for interacting with the CFD groups to suggest comparisons with experiments and with results of an adaptive grid solver.
- Co-PI Dr. Paul Sojka, Professor of Mechanical Engineering, is mentoring one of the graduate students and is responsible for supervising the spray measurements.
- Co-PI Scott Meyer, Managing Director of Maurice J. Zucrow Laboratories, is responsible for coordinating facility upgrades and for performing facility design reviews.
- Dr. Sameer V. Naik, Senior Research Scientist, is responsible for direct supervision of two graduate students involved in the experimental portion of the project.
- Graduate students Andrew Bokhart and Daniel Shin are responsible for performing the phase Doppler anemometry (PDA) measurements and for modifying the Rules & Tool Spray (RTS) test rig for operation at near-LBO conditions.
- Graduate student (until December 2019) and current research assistant professor, Hasti Veeraraghava Raju has conducted simulations with an adaptive grid solver and has performed comparisons with experimental results and results from the other CFD groups.

- Graduate student Neil Rodrigues contributes to the project by providing advice for the PDA measurements and technical editing.

Project Overview

The objectives of this project, as stated in the invitation for ASCENT COE Notice of Intent (COE-2014-29), are to "measure the spray characteristics of the nozzles used in the Referee Combustor used in Area 6 tests and to develop models for characterizing the atomization and vaporization of the reference fuels." We are conducting experiments within the joint experimental and modeling effort. The experimental tasks are being performed at Purdue University, and the modeling tasks are being performed by Professor Matthias Ihme's group at Stanford University, Prof. Suresh Menon's group at Georgia Tech, and Vaidya Sankaran's group at United Technologies Research Center (UTRC). Nader Rizk (Rolls Royce, retired) is developing spray correlations based on the measurements.

Purdue University has highly capable test facilities for measuring spray characteristics over wide ranges of pressure, air temperature, and fuel temperature. The experimental diagnostics applied in this project include PDA and high-frame-rate shadowgraphy. The atomization and spray dynamics for multiple reference and candidate alternative fuels have been characterized for the referee rig nozzle operating under near-LBO conditions. In the future, measurements will be performed for these fuels under operating conditions characteristic of HAR. A new fuel, IH^2 (Shell CPK-0), has been added to the test matrix and is being investigated under LBO and cold-start conditions.

Experimental Contributions

Objectives

The primary objectives of the work at Purdue University are to visualize and measure the nonreacting spray characteristics, including drop size distributions and axial velocity components of the sprays generated by a nozzle being used in the referee combustor rig in the Area 6 tests for standard and alternative aviation fuel candidates under a wide range of engine operating conditions. The upgraded Variable Ambient Pressure Spray (VAPS) test rig at Purdue allows us to investigate the spray characteristics for a variety of standard and alternative aviation fuels near LBO, engine cold-start, and high-ambient-pressure conditions. PDA has emerged as a technique of choice for obtaining fundamental drop size distribution and axial and radial velocity data for comparison with numerical simulations. The VAPS facility has been upgraded to allow us to test over the entire range of fuel and air temperatures and air pressures of interest.

The resulting data will be used for the development of spray correlations by consultant Nader Rizk and for the purpose of submodel development for detailed computer simulations being performed by Matthias Ihme, Suresh Menon, and Vaidya Sankaran. The experimental tasks are being performed at Purdue University, and the resulting data will be shared with FAA team members developing modeling, simulations, and engineering correlation-based tools.

The experimental data will support continued development and evaluation of engineering spray correlations, including the dependence of Sauter mean diameter (SMD), spray cone angle, and particle number density per unit volume on the fuel properties at fuel and air temperatures of interest. The experimental data will provide detailed statistical measurements for comparisons with high-fidelity numerical simulations of mixing and combustion processes. The prediction of the spatial distribution of the liquid fuel and the resulting vapor and breakdown components from the liquid fuels critically affect the ignition, flame-stabilization, and pollutant formation processes.

Major Accomplishments

Investigation at LBO Conditions

The representative diameters are used to characterize the spray: D_{10}, D_{32}, and *MMD*. D_{10} is the arithmetic mean diameter (first order mean) that represents the average drop diameter. The arithmetic mean diameter can be expressed as:

$$D_{10} = \frac{\sum N_i D_i}{\sum N_i}$$

where N_i is the number of droplets and D_i indicates the drop diameter. The subscription, i, indicates the drop size class.

D_{32} is a fifth order mean diameter that represents the ratio of drop volume to drop surface area. This is also called Sauter Mean Diameter (SMD). D_{32} is a representative diameter that typically used for drop size comparisons in mass transfer and reaction applications. The Sauter Mean Diameter (D_{32}) can be expressed as:

$$D_{32} = \frac{\sum N_i D_i^3}{\sum N_i D_i^2}$$

Lastly, *MMD* indicates the mass median diameter, which represents the diameter at which 50% of the total liquid volume is contained within smaller diameters. The expression for *MMD* is:

$$0.5 = \int_0^{MMD} f_3(D)dD$$

where, f_3 (D) indicates the volume probability density functions and *dD* is the drop size bin.

The mean axial drop velocity, U_z, measured by the PDA system was also used to represent the drop size velocity at different spray locations. The PDA system measures 20,000 sample droplets at each radial location within the spray, and U_z is the mean of 20,000 axial drop velocity values.

Effect of pressure drop

The pressure drop across the swirler ($\Delta P/P$) was observed to have a significant effect on the D_{10}, D_{32}, *MMD*, and the axial velocity U_z for both standard (Jet A) and alternative aviation fuels (C-1, C-5, C-7, and C-8). Figure 1 shows that D_{10}, D_{32}, and *MMD* decreased with increasing $\Delta P/P$ for all radial locations. The magnitude of the drop velocity was observed to increase for greater $\Delta P/P$, as shown in Figure 1d. Higher $\Delta P/P$ results in a higher atomizing gas velocity, which leads to greater inertial and aerodynamic forces to overcome the viscous and surface tension forces of the bulk liquid and, in turn, results in smaller drop diameters. The drop velocities near the center of the spray were negative, which confirms that a majority of the droplets near the center were traveling back toward the injector within the hollow cone. No significant variation was observed at r = 15 mm, where the transition of the spray from the hollow cone to the fuel cone exists. Similar trends in drop size and velocity as functions of $\Delta P/P$ were observed at the measurement planes (z) of 12.7 and 38.1 mm and for C-1, C-5, C-7, and C-8 fuels.

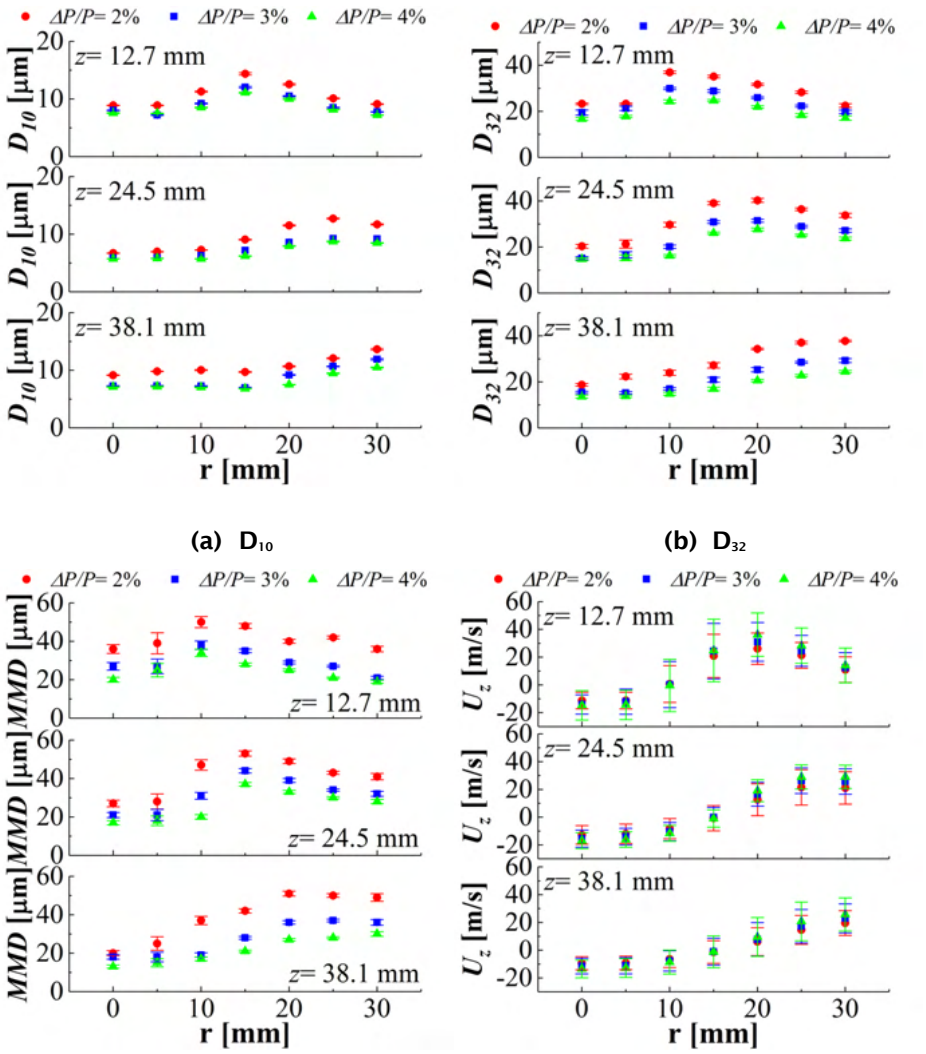

Figure 1. Drop diameter (D_{10}, D_{32}, *MMD*) and drop velocity (U_z) distributions for A-2 at pressure drop ($\Delta P/P$) = 2, 3, and 4% for measurement plane (z) = 12.7, 25.4, and 38.1 mm. D_{10} = arithmetic mean diameter; D_{32} = Sauter Mean Diameter; MMD = mass median diameter; r = radial location.

Effect of fuel injection pressure

The fuel injection pressure differential across the pilot nozzle, ΔP_{Pilot}, was varied to values of 1.72, 3.45, and 5.17 bar to investigate the effect of fuel mass flow rate on drop size and drop velocity. ΔP_{Pilot} dictates the total fuel mass flow rate through the pilot nozzle. The mass flow rates as measured by a Coriolis flow meter for each fuel injection pressure were 2.52, 3.56, and 4.59 g/s, respectively. Figure 2 shows D_{32} and U_z for the A-2 fuel. The effect of the fuel injection pressure on the mean drop size and velocity was found to be minimal. We considered that the variations in fuel injection pressure (1.72–5.17 bar) were not significant enough to affect mean drop size due to the dominating effect of the atomizing gas from the airblast component of the atomizer.

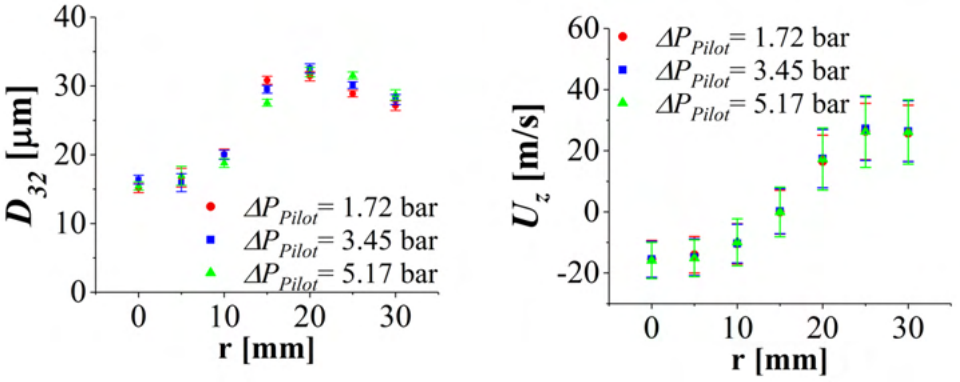

(a) D_{32} **(b) Uz**

Figure 2. Drop diameter (D_{32}) and drop axial velocity (U_z) with variation in fuel injection pressure (ΔP_{Pilot}). r = radial location.

Effect of fuel type

The effect of fuel type (A-2, C-1, C-5, C-7, and C-8) was investigated under LBO conditions for $\Delta P/P$ = 2, 3, and 4%. Figure 3 shows D_{32} and U_z for each fuel at the 25.4-mm measurement plane. The D_{32} measurement showed that C-7 formed the largest droplets and C-1 formed the smallest. We observed that the effect of viscosity on drop size was minimal, with approximately 60% variation in viscosity value among fuels at LBO conditions. The drop size trend, however, seemed to follow the surface tension near the spray edge (r >15 mm). The U_z measurements showed no significant variations among the fuels tested.

Figure 4 shows the relationships between line-of-sight D_{32} (D_{32o}) and viscosity and surface tension for all six fuels. D_{32o} is an averaged D_{32} value of the overall radial profile that is weighted by the volume flux at each radial location. As shown in Figure 4, no definitive relationship between the viscosity and drop size was observed. Drop size, however, tended to increase slightly with increasing surface tension. This was thought to be due to the high atomizing gas impingement angle onto the ligament that is formed at the prefilmer tip. It is hypothesized that if the atomizing gas impingement angle was lower than or parallel to the ligament axis, the effect of viscosity may not be negligible due to its resistance force to flow. However, if the gas impingement angle is close to normal, the surface tension is only responsible for the ligament breakup related to atomization energy. The model also successfully demonstrated drop size trends observed with viscosity and surface tension in Figure 4.

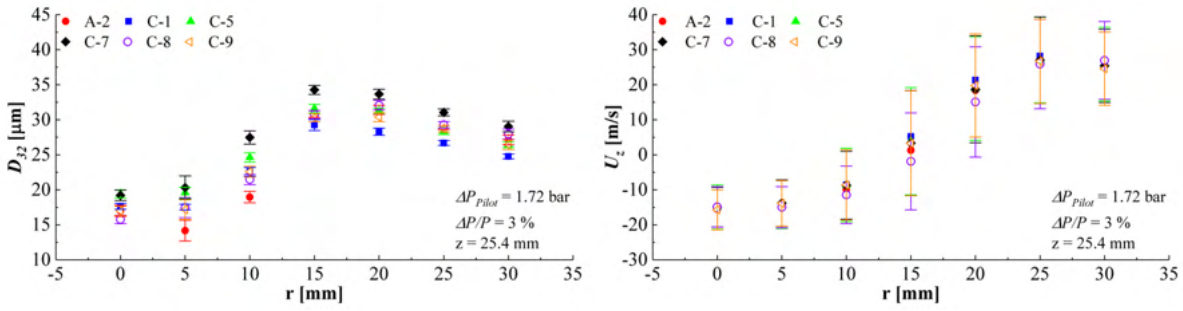

(a) D_{32} **(b) Uz**

Figure 3. Comparison of drop diameters (D_{32}) and drop velocities (U_z) for six fuels (A-2, C-1, C-5, C-7, C-8, and C-9) at lean blowout conditions. ΔP_{Pilot} = variation in fuel injection pressure; $\Delta P/P$ = pressure drop; z = measurement plane; r = radial location.

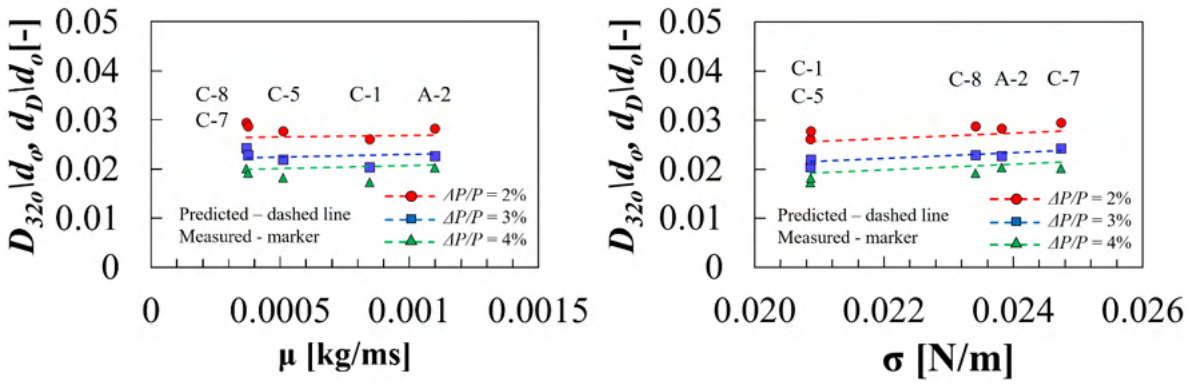

(a) D_{32o}/do and dD/do vs. viscosity **(b) D_{32o}/do and dD/do vs. surface tension**

Figure 4. Relationships between measured D_{32} and viscosity and surface tension for jet fuels A-2, C-1, C-5, C-7, and C-8. Dashed lines indicate the model predictions. D_{32o} = line of sight D_{32}; d_o = orifice diameter; d_D = predicted D_{32}; $\Delta P/P$ = pressure drop; μ = viscosity; σ = surface tension.

Investigation at Engine Cold Start Conditions

Effect of pressure drop

The pressure drop across the swirler ($\Delta P/P$) was found to have a significant effect on parameters D_{32} and U_z for the A-2, A-3, and C-3 fuels. Figure 5 shows the spatial distributions of D_{32} and U_z for pressure drops of 2, 3, and 4%, at a constant fuel injection pressure differential ($\Delta P/P$) of 1.72 bar and at a measurement plane (z) of 25.4 mm for A-2 and C-3 fuels. The air-to-liquid ratios of the atomizer for pressure drops of 2, 3, and 4% were calculated to be 12, 15, and 17, respectively. Drop size D_{32} was observed to decrease significantly as the pressure drop increased. The mean drop axial velocity, in contrast, increased in magnitude with increasing pressure drop. An increase in pressure drop results in a higher atomizing gas velocity, which corresponds to greater inertial and aerodynamic forces for the gas flow. This amplified the hydrodynamic instabilities of the bulk fuel and resulted in smaller droplets. Similar drop size and drop velocity trends were observed for A-3 fuel.

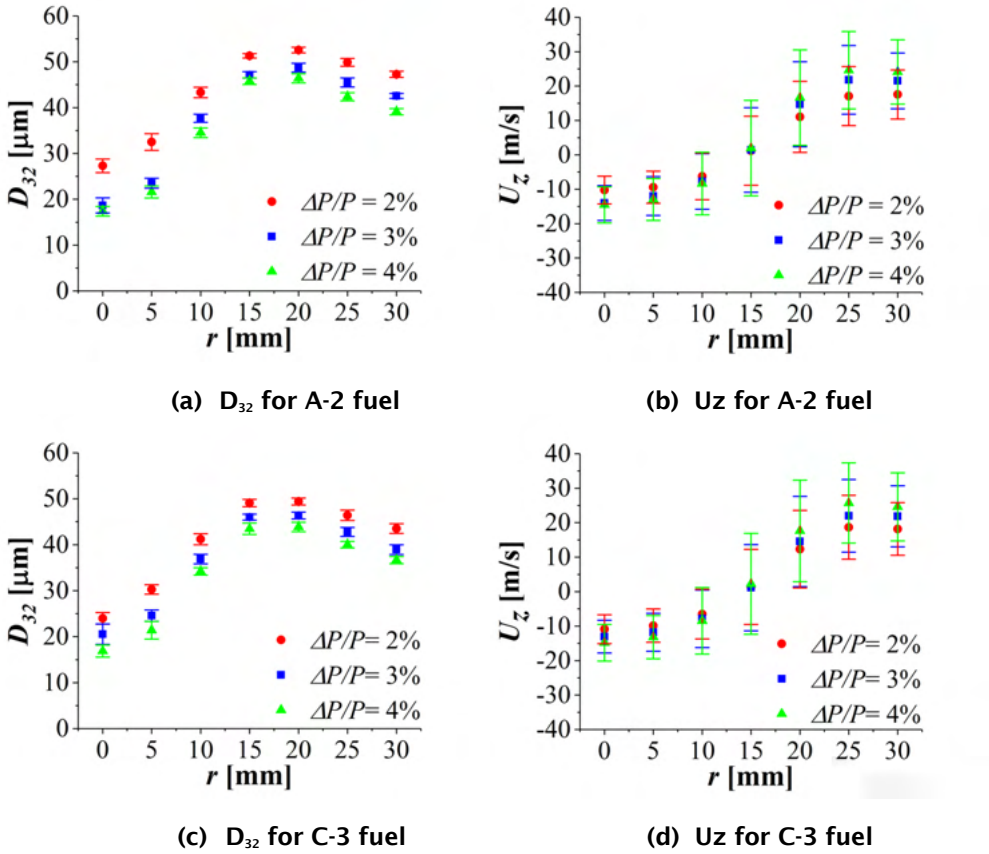

(a) D_{32} for A-2 fuel (b) Uz for A-2 fuel

(c) D_{32} for C-3 fuel (d) Uz for C-3 fuel

Figure 5. Comparisons of drop diameters (D_{32}) and drop velocities (U_z) for A-2 and C-3 fuels at $\Delta P/P$ = 2, 3, and 4%, ΔP_{Pilot} = 1.72 bar, T_{fuel} = 239 K, and T_{airbox} = 239 K for measurement plane (z) = 25.4 mm. ΔP_{Pilot} = variation in fuel injection pressure; $\Delta P/P$ = pressure drop; r = radial location; T_{fuel} = fuel temperature; T_{airbox} = airbox temperature.

Effect of fuel type

Three fuels (A-2, A-3, and C-3) were compared to investigate the effects of fuel properties on drop diameters and axial velocities. Figure 6 shows the comparisons of D_{32} and U_z for the three fuels at $\Delta P/P$ = 3% at the 25.4-mm measurement plane. The C-3 fuel had the highest viscosity value among the fuels and was expected to form larger droplets. However, it formed droplets with the smallest D_{32}. The largest D_{32} was observed for the A-3 fuel within the recirculation zone, whereas the A-2 and C-3 fuels formed droplets with similar D_{32} in the same region. The A-2 fuel was observed to form droplets with the largest D_{32} near the edge of the spray, and C-3 fuel formed droplets with the smallest D_{32}.

Figure 7 shows the relationship between the line-of-sight D_{32} (D_{32o}) and viscosity and surface tension for all three fuels under cold-start conditions. Based on these observations, we determined that the effect of surface tension dominated the effect of viscosity on drop sizes. The model (dashed lines) successfully demonstrated these drop size trends with viscosity and surface tension for three different pressure drop values.

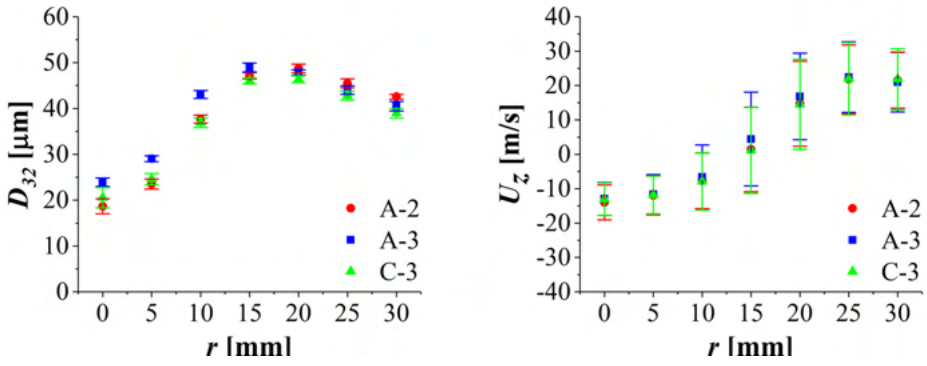

(a) D_{32} for A-2, A-3, and C-3 fuels **(b) Uz for A-2, A-3, and C-3 fuels**

Figure 6. Comparisons of drop diameters (D_{32}) and drop velocities (U_z) for A-2, A-3 and C-3 fuels at $\Delta P/P$ = 3%, ΔP_{Pilot} = 1.72 bar, T_{fuel} = 239 K, and T_{airbox} = 239 K for measurement plane (z) = 25.4 mm. $\Delta P/P$ = pressure drop; r = radial location; ΔP_{Pilot} = variation in fuel injection pressure; T_{fuel} = fuel temperature; T_{airbox} = airbox temperature.

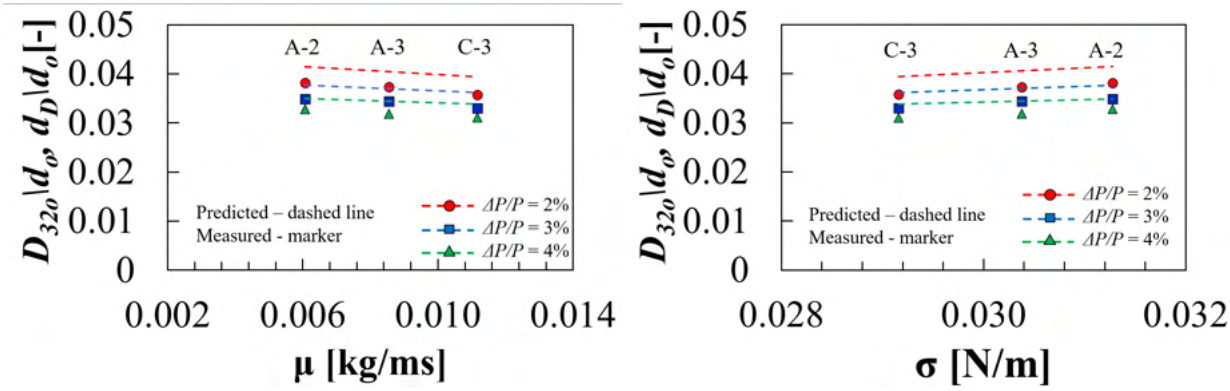

(a) D_{32o}/do and dD/do vs. viscosity **(b) D_{32o}/do and dD/do vs. surface tension**

Figure 7. Relations between measured D_{32} and viscosity and surface tension. Dashed lines indicate the model predictions. D_{32o} = light of sight D_{32} ; d_o = orifice diameter; d_D = predicted D_{32}; $\Delta P/P$ = pressure drop; μ = viscosity; σ = surface tension

Investigation at High Ambient Pressure Conditions

Effect of ambient pressure

Ambient pressure (P_{vessel}) was found to significantly affect mean drop size. As shown in Figure 8, a significant decrease in D_{32} was observed as P_{vessel} increased from 1 bar to 9.5 bar. However, the effect of P_{vessel} on drop diameters diminished with a further increase in P_{vessel}. Furthermore, the spray tended to have a monodisperse drop size at higher P_{vessel}. The greater inertial and drag forces on a droplet and ligament with increasing density of the ambient gas resulted in smaller droplets. The drop axial velocity was observed to be similar for all ambient pressures, as shown in Figures 8(b) and 8(d). However, droplets near the spray edge were observed to slow down with increasing pressure because they were more affected by the drag force. The hollow-cone region boundary was observed to be preserved at higher ambient pressure.

The effect of pressure drop ($\Delta P/P$) on D_{32} and U_z was observed to be significant at P_{vessel} = 5 bar, as shown in Figure 9 for A-2 fuel. The pressure drop was varied to values of 2, 3, and 6% at ΔP_{pilot} = 1.72 bar, T_{fuel} = 332 K, T_{airbox} = 394 K, and z = 25.4 mm. The D_{32} decreased with increasing $\Delta P/P$ and tended to be monodisperse across the radial locations at higher $\Delta P/P$. Drop axial

velocity was observed to increase with increasing $\Delta P/P$, as shown in Figure 9(b). Greater inertial force of the gas flow with increasing $\Delta P/P$ led to the formation of smaller droplets.

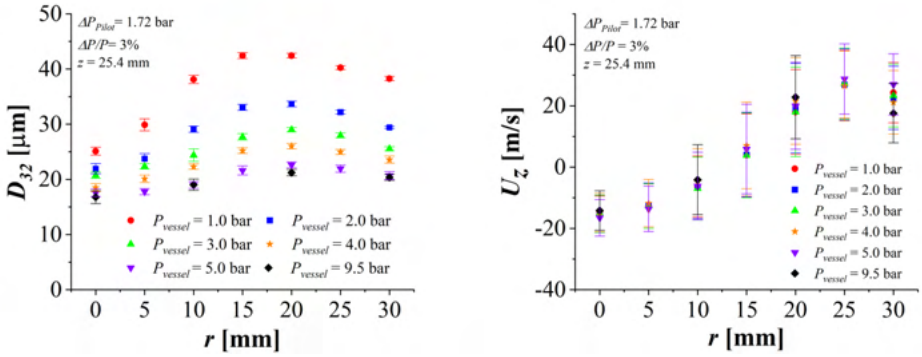

(a) D_{32}, A-2 **(b)** Uz, A-2

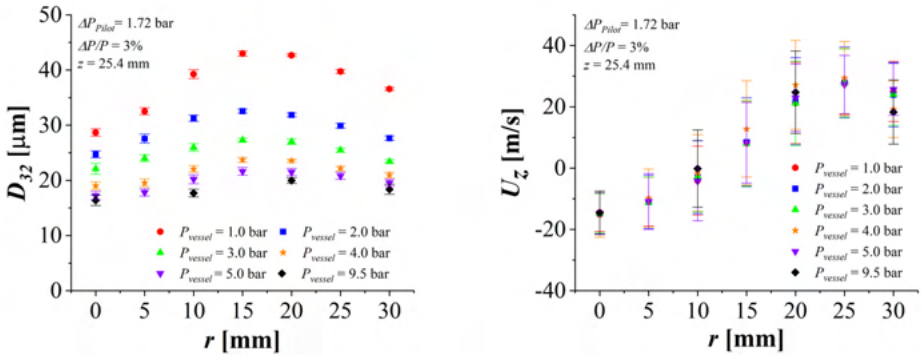

(c) D_{32}, C-5 **(d)** Uz, C-5

Figure 8. Comparisons of drop diameters (D_{32}) and drop velocities (U_z) for A-2 and C-5 fuels at P_{vessel} = 1,2,3,4,5, and 9.5 bar, $\Delta P/P$ = 3%, ΔP_{pilot} = 1.72 bar, T_{fuel} = 332 K, and T_{airbox} = 394 K for measurement plane (z) = 25.4 mm. P_{Vessel} = ambient pressure; ΔP_{Pilot} = variation in fuel injection pressure; $\Delta P/P$ = pressure drop; r = radial location ; T_{fuel} = fuel temperature; T_{airbox} = airbox temperature.

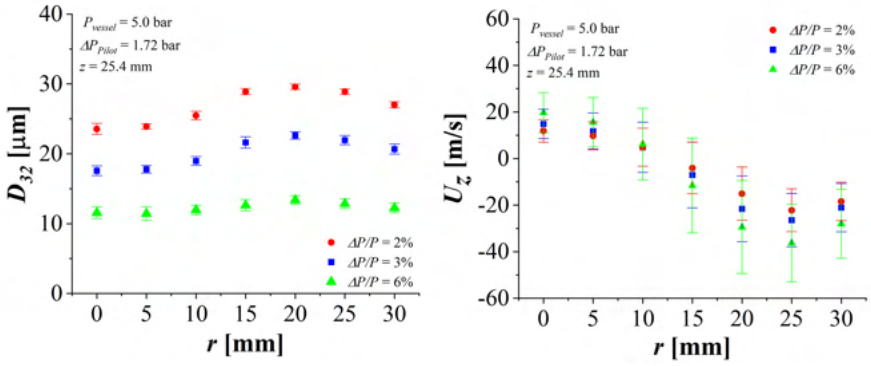

(a) D_{32} **(b) U_z**

Figure 9. Comparisons of drop diameters (D_{32}) and drop velocities (U_z) for A-2 fuel at $\Delta P/P$ = 2, 3, and 6 %, P_{vessel} = 5 bar, ΔP_{pilot} = 1.72 bar, T_{fuel} = 332 K, and T_{airbox} = 394 K for measurement plane (z) = 25.4 mm. P_{Vessel} = ambient pressure; ΔP_{Pilot} = variation in fuel injection pressure; $\Delta P/P$ = pressure drop; r = radial location; T_{fuel} = fuel temperature; T_{airbox} = airbox temperature.

Figure 10(a) shows the effect of ambient pressure on the drop size by comparing average drop size (D_{32o}/d_o) and predicted drop size (d_D/d_o) at different ambient pressures for A-2 and C-5 fuels. The effect of ambient pressure on drop size was observed to diminish as ambient pressure increased for both fuels. The model successfully demonstrated the drop size trend with increasing ambient pressure within ±20% error compared to measured drop sizes. Figure 10(b) shows the effect of pressure drop on drop size at elevated ambient pressure of 5 bar for A-2 fuel using dimensionless measured line-of-sight D_{32} (D_{32o}/d_o). The model was also able to demonstrate the drop size trend with increasing pressure drop.

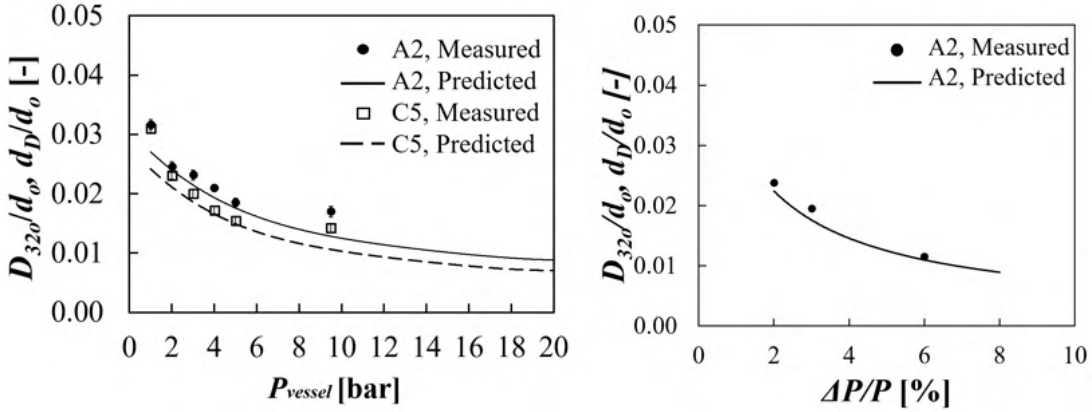

(a) D_{32o}/do and dD/do vs. P_{vessel} **(b) D_{32o}/do and dD/do vs. $\Delta P/P$**

Figure 10. Comparison of nondimensionalized measured average drop sizes (D_{32o}/d_o) and predicted drop size (d_D/d_o) at different ambient pressures and different pressure drops for A-2 and C-5 fuels at $\Delta P/P$ = 3%, ΔP_{pilot} = 1.72 bar, T_{fuel} = 332 K, and T_{airbox} = 394 K for measurement plane (z) = 25.4 mm. P_{Vessel} = ambient pressure; ΔP_{Pilot} = variation in fuel injection pressure; $\Delta P/P$ = pressure drop; T_{fuel} = fuel temperature; T_{airbox} = airbox temperature.

Liquid and vapor discrimination

Liquid and vapor discrimination analysis were performed using planar laser-induced fluorescence (PLIF) and Mie images. Figure 11 shows pairs of simultaneously captured PLIF (left) and Mie (middle) images and the normalized difference image

from PLIF and Mie images (right) at P_{vessel} = 1, 2, and 9.5 bar. Although the comparison between the Mie and PLIF images presented in this section is nonquantitative, it can be a useful approach to identify and distinguish liquid and vapor regions in the spray.

From Figures 11(b), 11(e), and 11(h), it can be seen that the number of droplets near the spray center increased at higher ambient pressure. This is thought to be due to an increased number of smaller droplets at higher ambient pressure being recirculated into the hollow cone region, increasing the number of scattering events and signals. Smaller droplets at P_{vessel} = 9.5 bar were observed to have a greater tendency to follow the gas flow compared with those observed at lower P_{vessel}, as shown in Figures 11(c), 11(f), and 11(i).

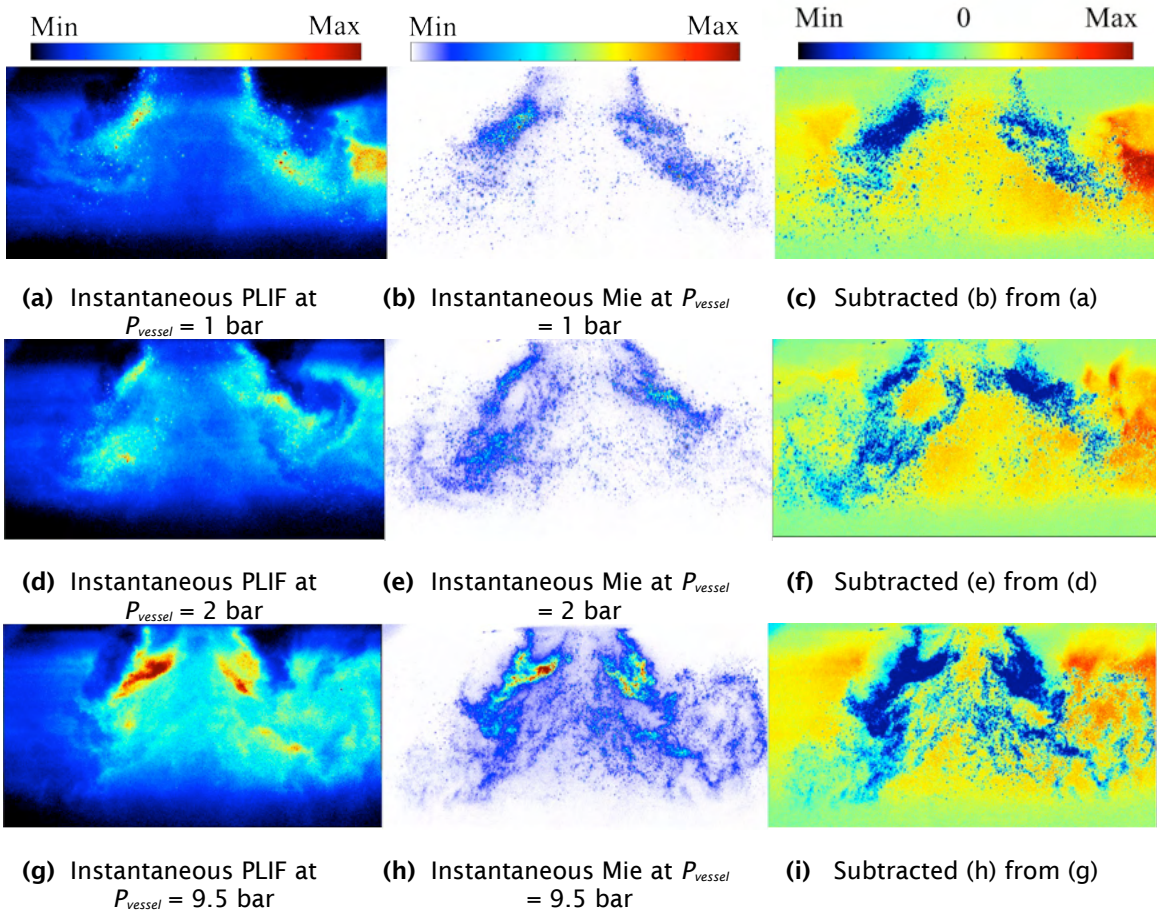

(a) Instantaneous PLIF at P_{vessel} = 1 bar **(b)** Instantaneous Mie at P_{vessel} = 1 bar **(c)** Subtracted (b) from (a)

(d) Instantaneous PLIF at P_{vessel} = 2 bar **(e)** Instantaneous Mie at P_{vessel} = 2 bar **(f)** Subtracted (e) from (d)

(g) Instantaneous PLIF at P_{vessel} = 9.5 bar **(h)** Instantaneous Mie at P_{vessel} = 9.5 bar **(i)** Subtracted (h) from (g)

Figure 11. Liquid–vapor discrimination A-2 fuel at P_{vessel} = 1, 2, and 9.5 bar, $\Delta P/P$ = 3%, ΔP_{pilot} = 1.72 bar, T_{fuel} = 332 K, and T_{airbox} = 394 K. PLIF = planar laser-induced fluorescence; P_{Vessel} = ambient pressure; ΔP_{Pilot} = variation in fuel injection pressure; $\Delta P/P$ = pressure drop; T_{fuel} = fuel temperature; T_{airbox} = airbox temperature.

Publications

Bokhart, A. J., Shin, D., Rodrigues, N. S., Lucht, R. P., Gore, J. P., & Sojka, P. E. (2018) Spray characteristics of a hybrid airblast pressure-swirl atomizer at near lean blowout conditions using phase doppler anemometry [Presentation]. AIAA SciTech 2018 Forum, Atlanta, GA.

Bokhart, A. J., Shin, d., Gejji, r., Buschhagen, T., Naik, S. V., Lucht, R. P., Gore, J. P., Sojka, P. E., & Meyer, S. E. (2017). Spray measurement at elevated pressures and temperatures using phase doppler anemometry [Presentation]. AIAA SciTech 2017 Forum, Grapevine, TX.

Shin, D., Bokhart, A. J., Rodrigues, N. S., Gore, J. P., Sojka, P. E., & Lucht, R. P. (2019). Non-reacting spray characteristics for alternative aviation fuels at near lean blowout conditions. Journal of Propulsion and Power, *36*(3), 323–334.

Shin, D., Bokhart, A. J., Rodrigues, N. S., Lucht, R. P., Gore, J. P., & Sojka, P. E. (2019). Experimental study of spray characteristics at cold start and elevated ambient pressure using hybrid airblast pressure-swirl atomizer [Presentation]. AIAA SciTech 2019 Forum, San Diego, CA.

Shin, D., Rodrigues, N. S., Bokhart, A. J., Gore, J. P., Sojka, P. E., & Lucht, R. P. (2020). *Spray characteristics of standard and alternative aviation fuels at cold start conditions* [Manuscript submitted for publication].

Shin, D., Hasti, V. R., Rizk, N., Bokhart, A. J., Rodrigues, N. S., Corber, P. A., Sojka, P. E., Lucht, R. P., & Gore, J. P. (2021). *Chapter VIII. Spray characteristics of conventional and alternative fuels,* Fuel Effects on Operability of Aircraft Gas Turbine Combustors, Edited by Meredith Colket and Joshua Heyne, ISBN: 978-1-62410-603-3, Progress in Astronautics and Aeronautics, American Institute of Aeronautics and Astronautics, 2021. https://doi.org/10.2514/4.106040

Shin, D., Aman, S., & Lucht, R. P. (2021). *Spray characteristics of standard and alternative aviation fuels at high ambient pressure conditions* [Manuscript in preparation].

Summary: Modeling and Simulation of Fuel Effects on Lean Blowout (LBO)

Objectives

The main objective of the computational research at Purdue was to establish modeling and simulation methodology to predict the fuel composition effects on LBO in the referee combustor at engine-relevant conditions. The CFD methodology to predict LBO in a liquid-fueled gas turbine combustor is not well established in the literature. As part of this National Jet Fuel Combustion Program (NJFCP) FAA project, we have focused on developing CFD methodology, including all the hardware features as-it-is on the real engine combustor. The successful demonstration of these computational tools will help identify the best CFD models and best practices to predict the fuel sensitivity to LBO limits in a swirl-stabilized gas turbine combustor. Another objective was to demonstrate the methodology for conventional Jet A fuel (denoted A-2) and an alternative aviation fuel (C-1). The experimental data from the Maurice J. Zucrow Laboratory (Purdue) were used to determine the spray boundary conditions. The reacting spray measurements, OH* chemiluminescence from the referee experiments at University of Illinois Urbana-Champaign (UIUC), Illinois, and the LBO equivalence ratios from the rig tests at University of Dayton Research Institute/Air Force Research Laboratory (UDRI/AFRL), Ohio, were utilized to evaluate the CFD models. Then, we used the results from successful high-fidelity large-eddy simulations (LES) to understand flame structure under stable flame conditions and during blowout and to identify markers for early detection of combustion instabilities and LBO. This research effort also aimed to identify new measurements for model validation.

Accomplishments

Computational method

The Reynolds Averaged Navier-Stokes (RANS) and LES were performed for the referee combustor using the finite volume-based compressible CFD solver CONVERGE. The gas-phase equations are described using an Eulerian approach, and the liquid spray was modeled with discrete injections of droplets using a Lagrangian approach. The subgrid stress tensor terms in the momentum equations were modeled using a non-viscosity-based one-equation model to obtain closure. Two different combustion models—namely, the detailed chemistry solver utilizing the laminar finite-rate chemistry (FRC) model and flamelet approach using the FGM model—were evaluated for LBO predictions. The HyChem kinetic models and compact kinetic models based on fuel surrogates were used to represent chemical reactions. The FGM model accounts for the effects of turbulence on reaction rates via a joint probability density function of the mixture fraction, the mixture fraction variance, and a reaction progress variable. A fully automated on-the-fly meshing strategy, combined with the cut-cell Cartesian method and adaptive mesh refinement (AMR), was employed, and the mesh parameters were selected based on a grid sensitivity study. More than 90% of the turbulent kinetic energy is resolved in the combustor region with appropriate mesh size and distribution. Additional details on the boundary conditions and the spray can be found in Hasti et al. (2018; 2018).

The spray is represented by an ensemble of six ring injectors, each with prescribed cumulative distribution functions for droplet diameter, average velocity, cone angle, mass flow rate, and parcel number. The spray boundary conditions (droplet diameter, average velocity, and cone angle) at 2 mm from the nozzle exit were obtained from the PDA measurements (from detailed measurements described in our experimental contribution section) at 25.4 mm from the deflector plate. An ensemble of six ring injectors, each with its own droplet size and velocity distribution, represents the nozzle. Taylor analogy secondary breakup and dynamic drag models were used to estimate the secondary breakup and resulting spray droplet

dynamics. A droplet dispersion model was used to include the effects of the sub-grid-scale flow field on the discrete parcels. The droplet evaporation rates were calculated using the Frossling correlation based on the laminar mass diffusivity of the fuel vapor, mass transfer number, and Sherwood number. The prescribed fuel properties were set as those determined for the A-2 and C-1 fuels.

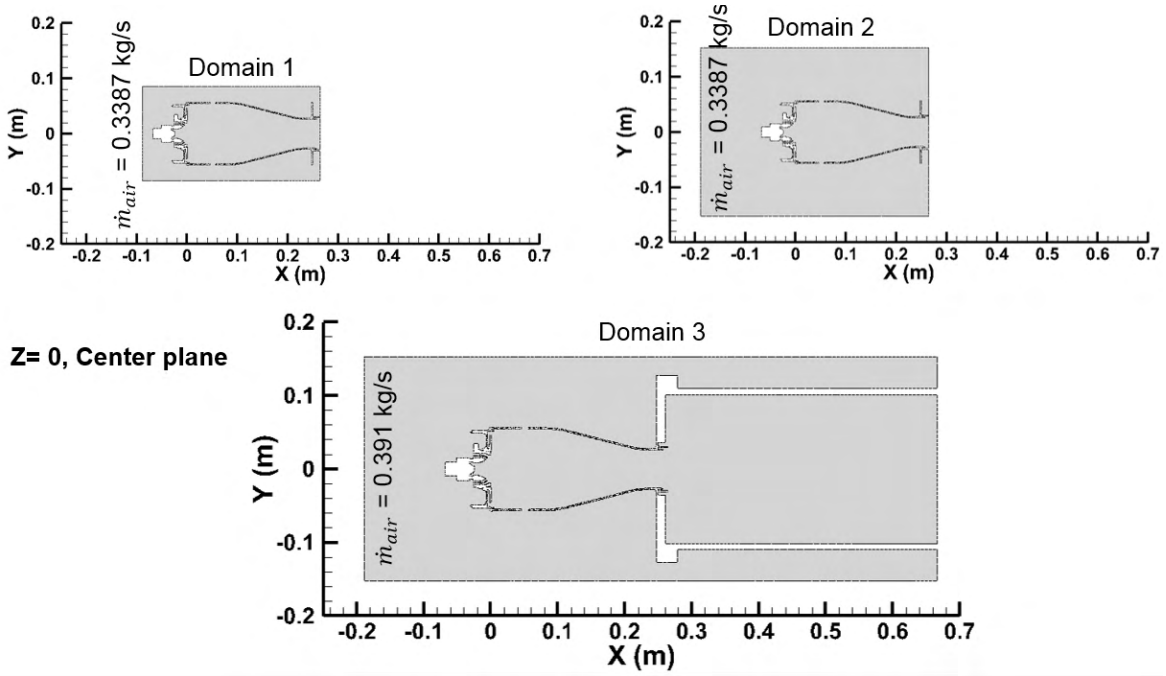

Figure 12. Comparison of computational domains at the Z=0, Center plan for the three computational domains. $\dot{m}_{air}$ is the mass flow rate of air.

Nonreacting flow simulations were carried out for the referee combustor with three different computational domains as shown in Figure 12. The flow splits comparison between these three domains is shown in Table 1. This sensitivity study was carried out to understand the sensitivity of the plenum size on the combustor flow splits and flow field in the primary zone. For domain 1, the dilution jets in the first row enter the combustor at a higher velocity because of the smaller width of the annulus and therefore show an $8°$ greater angle. The results showed that domain size does not have a significant effect on flow patterns or velocity magnitudes in the critical primary flame stabilization zone. This zone is dominated by swirling flow. Domain 1 was used for the reacting LES, and the computational domain external to the combustor was reduced in order to focus on better resolving the complex swirling flowfield with fine mesh in the combustor region and gridding through the cooling holes in the combustor. Reductions in the length of the plenum upstream of the swirler section and the annular region beyond the combustor walls, and elimination of the large circular outlet section beyond the combustor exit were not expected to significantly affect the highly swirling flowfield in the primary zone. Results of the cold-flow simulations showed that the flow features of the primary zone in the vicinity of the injector were indeed insensitive to the reduced plenum size for domain 1. The 3-dimensional view of the domain 1 with a swirler and 2-dimensional cross-section at Z=0 are shown in Figure 13. The flow through all passages, including tiny effusion holes on the liners, was resolved in this CFD model. The computational grid for flow simulations with all passages open is shown in Figure 14. The grid is locally refined in the regions with the steepest gradients and is relatively coarse in sections with weaker gradients, based on AMR.

Table 1. Comparison of flow splits.

	Exp (g/s)	Domain 1 Non-Reacting (g/s)	Domain 1 Reacting A2-0.096 (g/s)	Domain 2 Non-Reacting (g/s)	Domain 3 Non-Reacting (g/s)
Dilution Row 1	39.5	45.22	46.3	47.03	47.45
Dilution Row 2	45.4	50.01	52.4	50.57	51.27
Total swirler	60.7	75.37	72.9	73.12	74.17
Radial swirler	14.3	15.56	14.7	15.68	15.34
Axial int. swirler	18.9	25.18	23.8	23.92	24.93
Axial ext. swirler	24.6	32.37	31.9	31.3	31.64
Swirler cooling	2.9	2.25	2.3	2.22	2.24
Effusive plate	245.4	167.66	166.7	164.82	210
Total (sum)	391	338.26	338.3	335.54	382.89

LBO simulation approach

LES were performed for a global equivalence ratio (Φ) of 0.096, which was experimentally found to produce stable combustion. From this condition, the fuel flow rate was reduced in a gradual stepwise manner; larger time steps were initially applied, and the flow rate steps were progressively reduced as impending blowout behavior was observed. The simulations were run with a fixed global equivalence ratio for at least two flow-through durations of approximately 30 ms. The fixed equivalence ratio was maintained beyond 30 ms if a quasi-steady heat release rate was not reached within either of those limits. The heat release rate was used as a criterion for identifying LBO. The global equivalence ratio steps resulting from this process are plotted in Figure 15 as a function of time for fuels A-2 (left) and C-1 (right). The experimental data shown by red filled circles indicate that the C-1 fuel blows out at a higher equivalence ratio than the A-2 fuel. The evolutions of the heat release rate for varying equivalence ratios and for two fuels with the FGM combustion model are shown in Figure 16. The flame is initially stable; subsequently, a steady decrease followed by a sharp reduction in the heat release rate is observed for both fuels. The heat release rates reach a steady state before the next step. In this figure, the dotted black line shows the mean heat release rate, and the dotted pink line shows the ideal heat release rate.

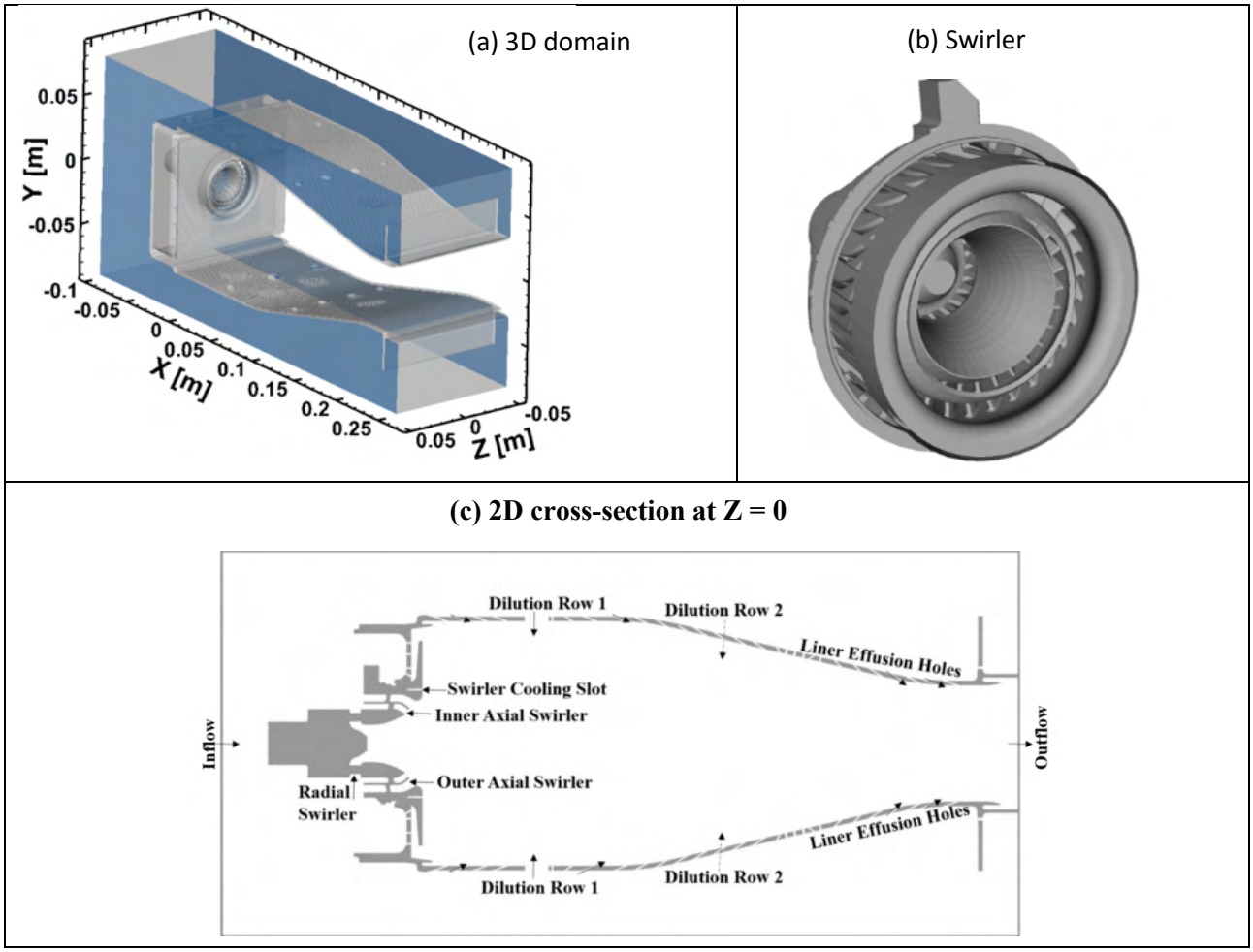

Figure 13. (a) Three-dimensional (3D) computational domain, (b) magnified view of the 3D swirler, and (c) magnified view of the 2-dimensional cross-section at Z=0 (mid-plane).

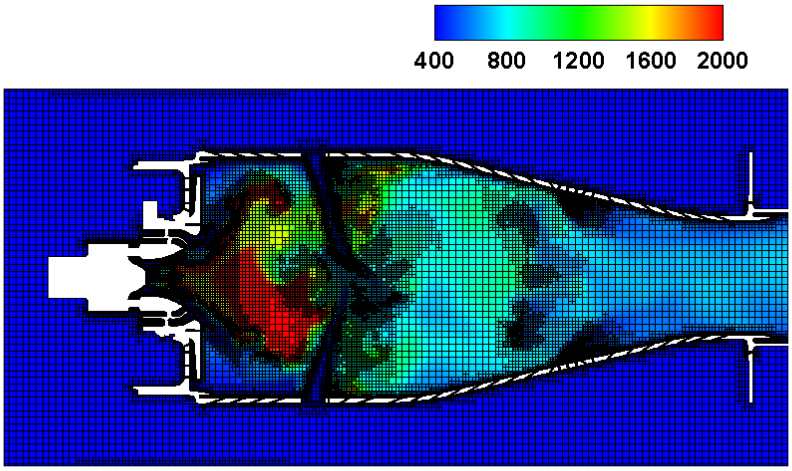

Figure 14. Computational grid with adaptive mesh refinement (AMR) on the mid-plane (Z=0) of the referee combustor for a reacting case with the flamelet-generated manifold (FGM) combustion model, with colored temperature [K] contours.

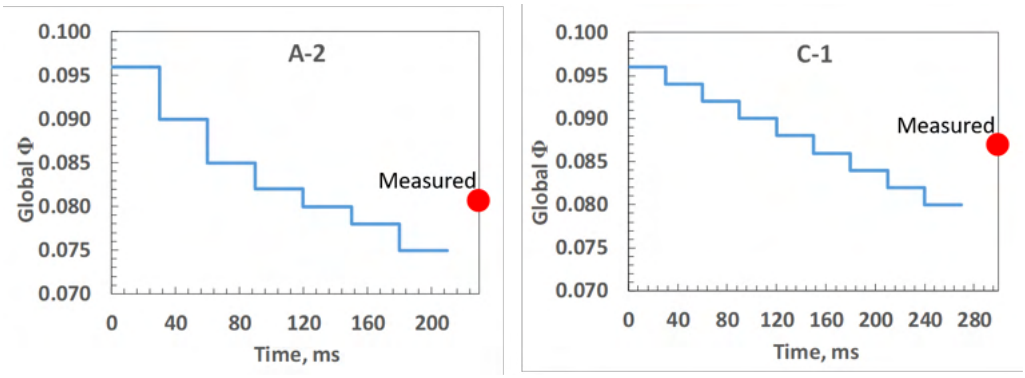

Figure 15. Staged fuel ramp-down approach for lean blowout (LBO) prediction using A-2 and C-1 fuels. The red dot represents the measured LBO global equivalence ratio (Φ).

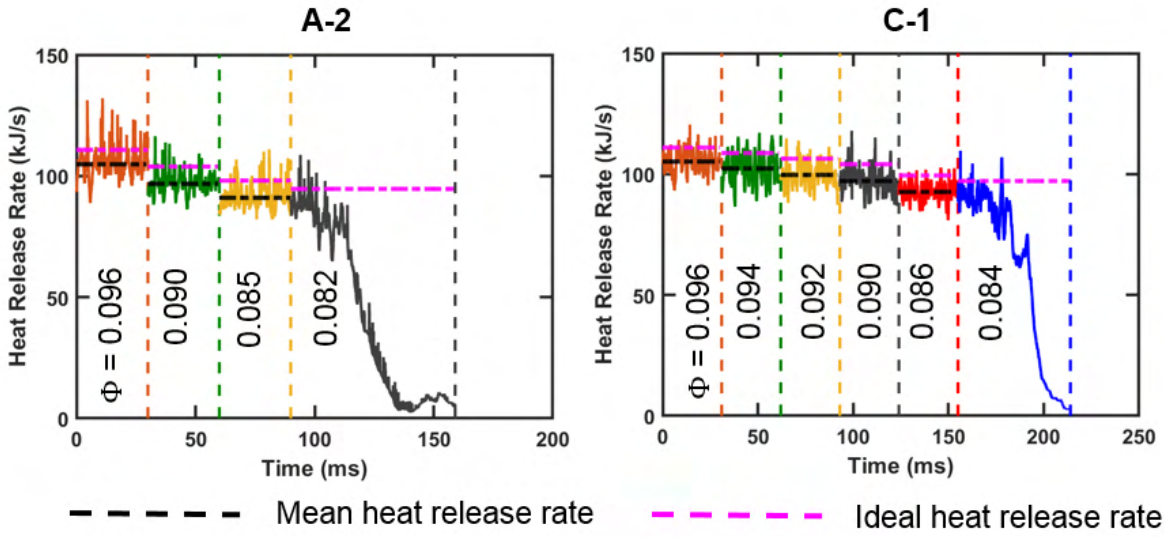

Figure 16. Heat release rate calculation with the flamelet-generated manifold (FGM) combustion model for A-2 and C-1 fuels. Φ = global equivalence ratio.

Reacting spray comparison under near-LBO conditions

Spray statistics were collected via LES calculations at a stable operating point over two flow-through durations. The averaging process over two flow-through durations was started after the flame and heat release rate reached a quasi-steady state. Figure 17 shows the experimental data and predicted droplet statistics as a function of radial distance for the FRC and FGM combustion models at four axial stations. The fuel spray exhibited a pattern with smaller-diameter droplets near the hollow cone surface 10 mm downstream of the nozzle exit. This distribution widened in the radial direction toward the downstream locations, with larger droplets toward the center and smaller droplets in the outer regions. The two combustion models satisfactorily captured this trend for both fuels, and better agreement with the experiments was observed for the downstream locations. The axial and radial velocities increased away from the center and decreased with increasing spray cone angle. These trends were accurately captured for the near-nozzle regions as well as the downstream regions for both fuels. Overall, the Lagrangian spray setup accurately captures spray breakup and evaporation.

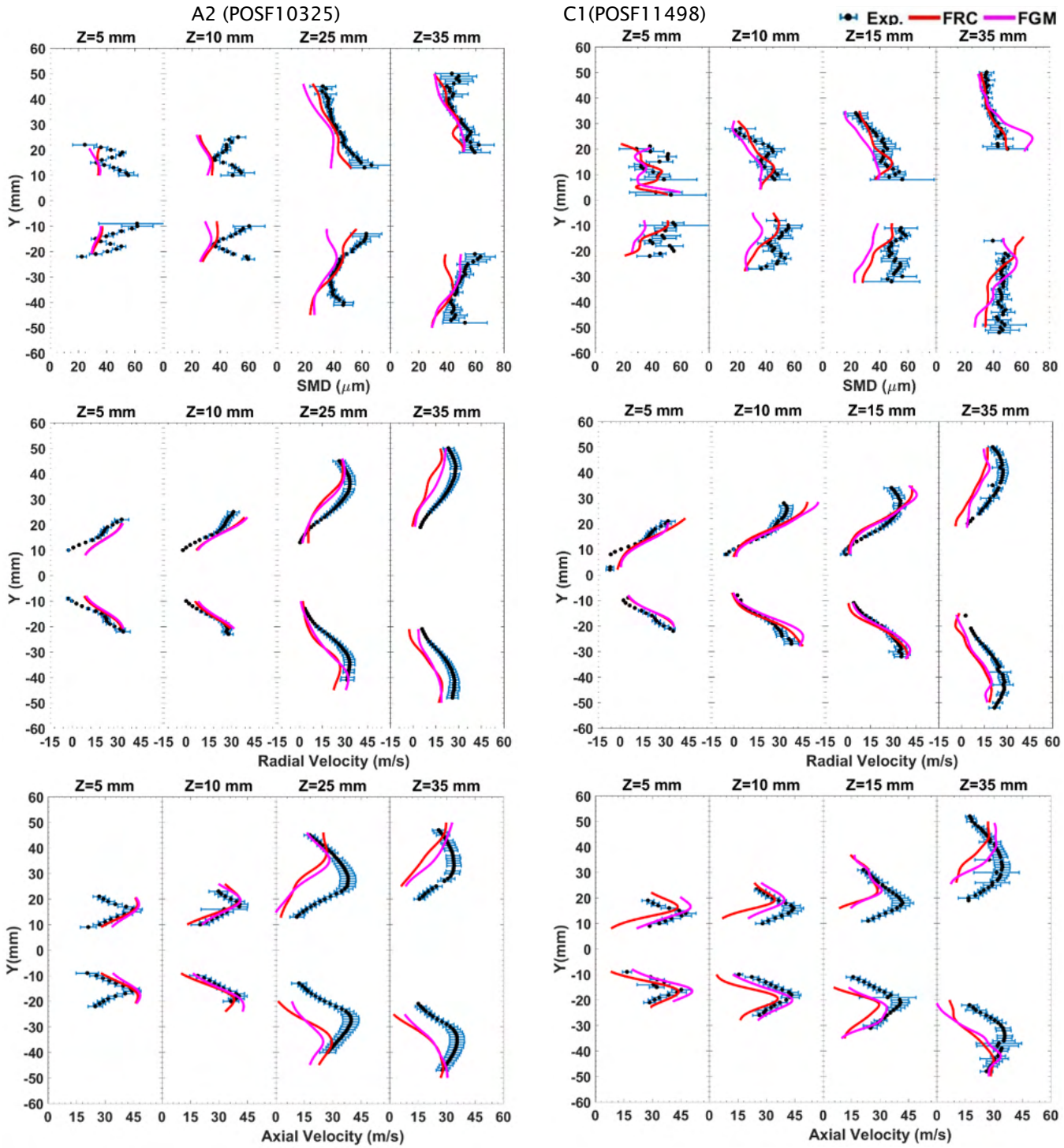

Figure 17. Comparison of spray statistics and phase Doppler anemometry (PDA) data for a stable flame at global equivalence ratio Φ = 0.096. FRC = finite-rate chemistry model; FGM = flamelet-generated manifold model; SMD = Sauter mean diameter.

Flame shape comparison

OH* chemiluminescence data from the UIUC experiments were used to compare the line-of-sight average OH mass fraction from LES for four kinetic mechanisms and two combustion models. The results for the detailed, skeletal, reduced, and compact mechanisms are displayed in Figure 18, alongside the experimentally observed OH* chemiluminescence. The results from the detailed, skeletal, and reduced mechanisms were qualitatively similar, and the experimental data (OH* chemiluminescence) and detailed mechanism calculations (OH) showed similar spreads in the radial and axial directions. However, it must be noted that these comparisons are qualitative. The experimental images are based on false color and do not indicate a quantitative measurement of the OH field. The horizontal position of 0 mm corresponds to the deflector plate. OH formation marks the high-temperature heat release region, which extends 50 mm downstream of the deflector plate and corresponds to the downstream location of the first row of dilution holes. This area is the stable region of the swirl-stabilized flame and exhibits a truncated cone shape, with regions of high OH/heat release corresponding to the cone angle of the hollow spray cone. This trend indicates strong burning and heat release near the spray cone surface downstream of the swirl cup. The A-2 fuel exhibited a higher degree of asymmetry in OH* for this configuration and measurement. These regions of intense heat release were qualitatively captured by all four chemistry mechanisms. The flame shape computed for the FGM combustion model showed a stronger and larger reaction zone compared with the FRC model.

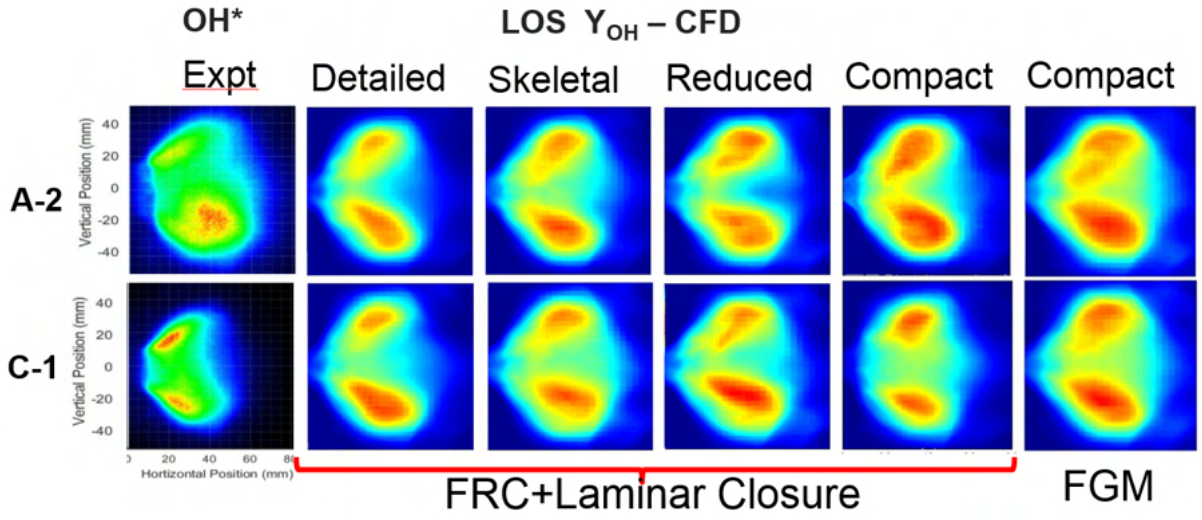

Figure 18. Line-of-sight (LOS) average OH mass fraction (Y_{OH}) obtained from large-eddy simulations (LES) compared with experimental (Expt.) OH* obtained from chemiluminescence. FRC = finite-rate chemistry model; FGM = flamelet-generated manifold model. CFD = computational fluid dynamics.

LBO equivalence ratio comparison

The LBO trends for both fuels were compared with experimental results in Figure 19. The C-1 fuel was shown to blow out at a higher equivalence ratio compared with A-2 in the experiments. This LBO dependence on the fuel's physical and chemical properties is very complex. The simulations with the FRC and FGM combustion models captured accurate LBO trends and relative behaviors for each fuel. However, the FGM model predicted that LBO would occur at a lower equivalence ratio compared with the FRC model because of the stronger flame root and larger reaction zone, as shown in Figure 20.

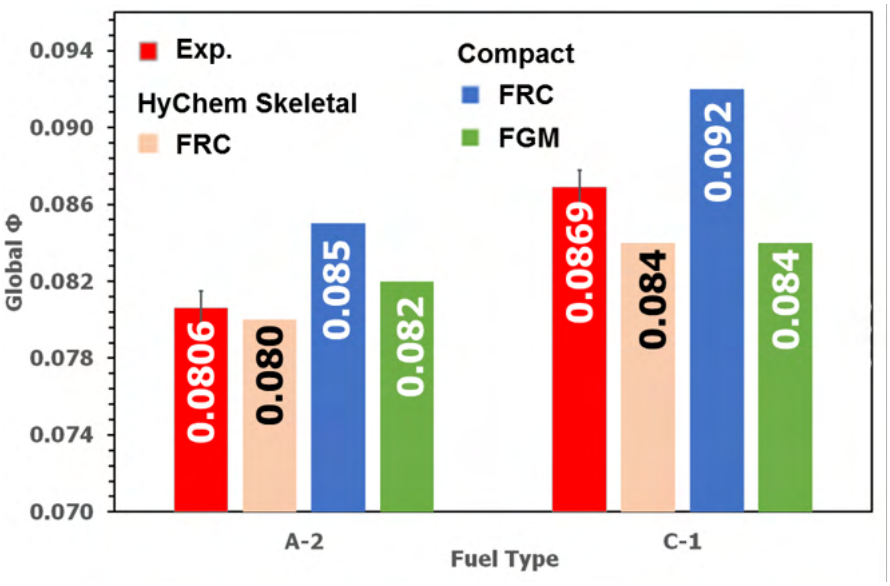

Figure 19. Comparison of lean blowout (LBO) global equivalence ratio (Φ) with experimental data for two different mechanisms—HyChem Skeletal and Compact—and two combustion models—finite-rate chemistry (FRC) and flamelet-generated manifold (FGM).

Evaluation of combustion models

The computed velocity, temperature, and mean OH mass fraction contours are compared for the FRC and FGM combustion models in Figure 20. The results for the FRC model show a pointed flame root and a smaller reaction zone, whereas the FGM model results show a stronger flame root and a much larger reaction zone. However, experimental validation data would be highly beneficial to verify the computational model results and to obtain further enhancements.

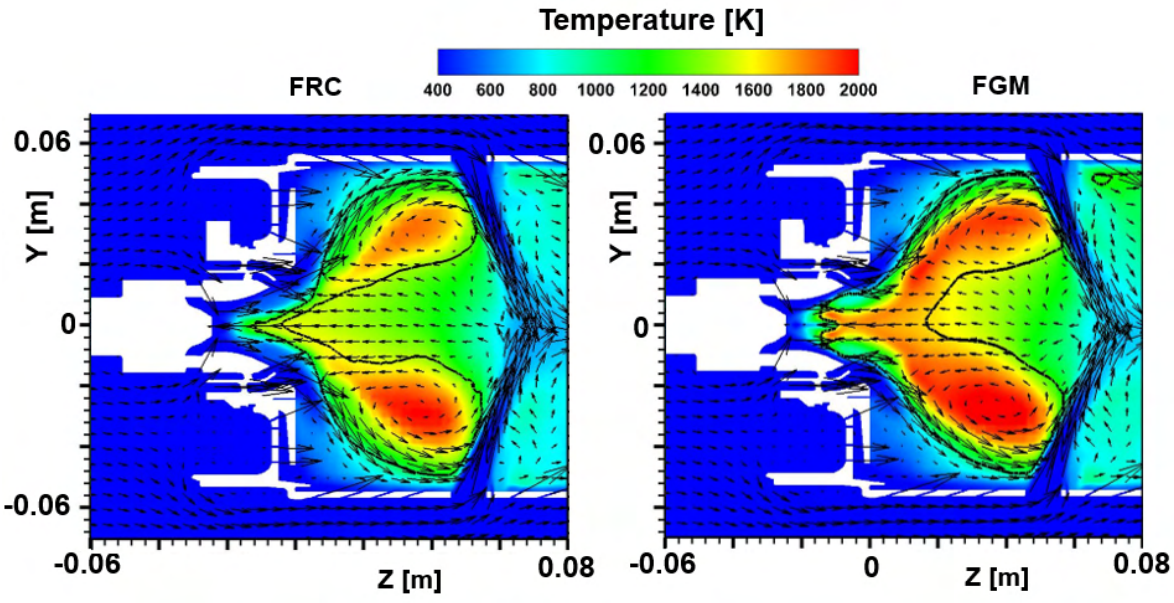

Figure 20. Comparison of temperature (filled contours), velocity (vectors), and an isocontour for a mean OH mass fraction of 5e-04 (black line) for C-1 fuel. FRC = finite-rate chemistry model; FGM = flamelet-generated manifold model.

Flame structure analysis under stable conditions and during LBO

The LES results from the HyChem skeletal mechanism were chosen for understanding the flame extinction process during LBO for the A-2 and C-1 fuels. Qualitative analysis of the flame during LBO is shown in Figure 21. Instantaneous temperature contour plots at the combustor mid-plane are shown on the left for both fuels, and corresponding formaldehyde mass fractions are shown on the right. The primary recirculation zone corresponds to the region of intense heat release rate. These regions correspond to the high OH formation regions described in the previous section. For A-2 fuel, after the final step-down, at an equivalence ratio of 0.080, a lifted flame was observed to stabilize inside the swirler cup region within the 0 to 5 ms window. Formaldehyde was observed to form very close to the nozzle tip and to follow the spray regions. Formaldehyde is oxidized to form the high-temperature regions. As time progressed, the flame stabilization point started to move in the axial direction and a remarkable shift in the CH_2O regions was observed, away from the nozzle tip. Finally, by 15 ms, the heat release in the primary recirculation region decreased considerably, with a considerable shift of CH_2O formation in the downstream regions. Finally, the flame was observed to blow out by 25 ms. A similar trend was observed for the C-1 fuel, but at a much higher global equivalence ratio of 0.084. The C-1 fuel had significantly greater CH_2O formation, even at 0 ms. To summarize these plots overall, the flame was observed to shift downstream as LBO was approached, along with downstream movement of intermediate species. The reduction of heat release rates and overall temperatures led to partial oxidation of these intermediate species, which is shown as a corresponding downstream shift in the contour plots.

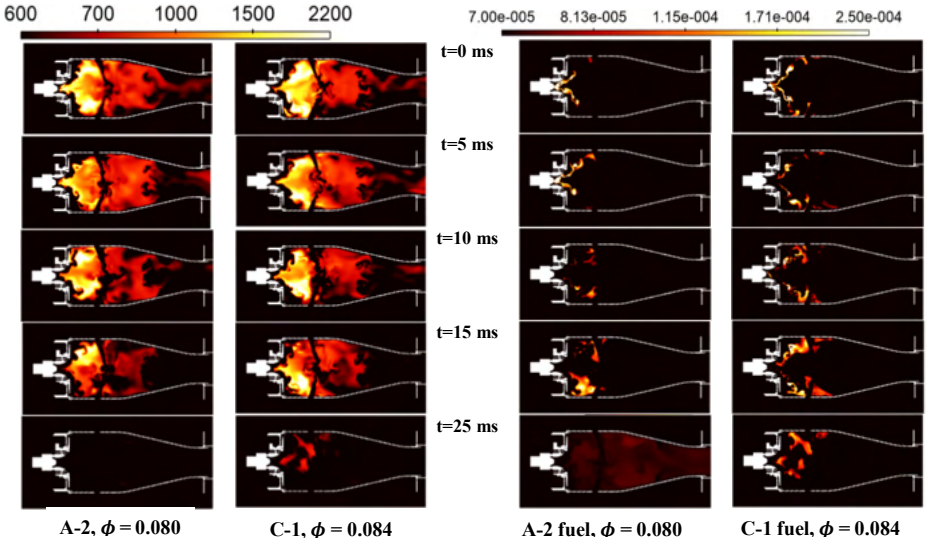

Figure 21. Instantaneous temperature [K] contour plots (left) at the combustor mid-plane and formaldehyde mass fractions (right) for A-2 and C-1 fuel during lean blowout. Φ = global equivalence ratio.

To understand flame stabilization and key factors governing LBO limits, we analyzed species formation in the mixture fraction space in the primary zone of the combustor. These are reported in Figure 22. The aim was to identify key markers or events that are universal, with respect to different fuels. Temperatures from the primary zone (upstream of the primary dilution holes) were isolated from the 3D CFD domain and further filtered based on their axial velocities. Computational cells that had axial velocities in the negative direction were selected for analysis. Because this was a nonuniform grid, these points were weighted with their respective cell volumes. These sets of points represent the recirculating fluid that flows from the high-temperature regions toward the base of the flame. Each point in the T-Z space is colored by CH_2O mass fraction. The red dotted line corresponds to the stoichiometric mixture fraction. These data points were also reported for the stable configuration at 0.096. We first considered the stable operating point for A-2. CH_2O was observed to form in the rich regions in the temperature range of 1000 to 1600 K. These regions were subsequently oxidized in the high-temperature regions. After a series of step-downs in equivalence ratio to 0.080, CH_2O formation shifted toward the richer regions, highlighted by the dotted lines. This shift indicated partial oxidation of the HC fuel due to a global reduction in heat release and corresponding temperatures. The C-1 fuel, in contrast, indicated relatively higher CH_2O concentrations in the rich regions, even for the stable operating point. This is an early indication of both partial oxidation and the likelihood of the flame

blowing out at relatively higher equivalence ratios. As expected, as the equivalence ratios were reduced, formaldehyde formation shifted to the richer regions, indicating partial oxidation and subsequent flame blowout by 15 ms. The higher concentration of intermediates in the rich regions can be attributed to the lowered temperature and a corresponding decrease in oxidation rates of intermediate species. The reduction in heat release rate (HRR) and overall temperatures further leads to a reduction in the overall evaporation efficiency, which finally leads to a blowout. The oxidation of the intermediate species to high-temperature radicals and saturated combustion products is the step that has a huge impact on LBO limits.

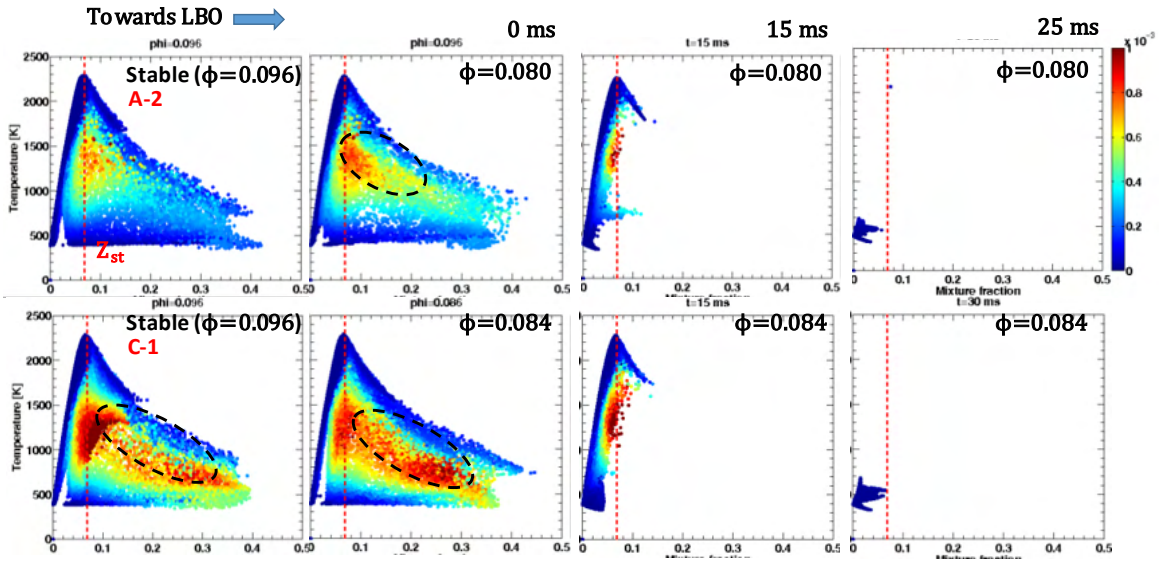

Figure 22. Temperature versus mixture fraction scatterplots for A-2 fuel (top) and C-1 fuel (bottom) sampled from the primary zone. Colored with CH_2O mass fraction. LBO = lean blowout; Φ = global equivalence ratio; Z_{st} = stoichiometric mixture fraction.

The intermediate radical OH is formed in the high-temperature stoichiometric regions and does not shift with lower global equivalence ratios, as shown in Figure 23. This study showed that the trend of increasing concentrations of intermediate species in rich regions is an important marker during the LBO process.

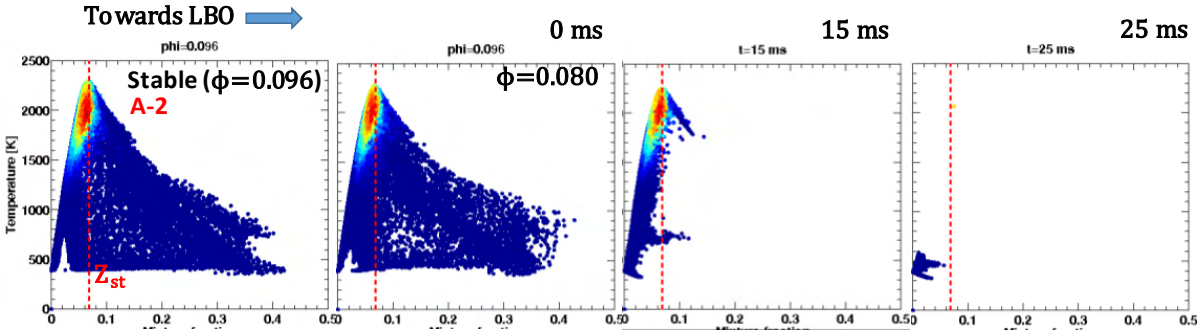

Figure 23. Temperature versus mixture fraction scatterplots for A-2 fuel sampled from the primary zone. Colored with OH mass fraction. LBO = lean blowout; Φ = global equivalence ratio; Z_{st} = stoichiometric mixture fraction.

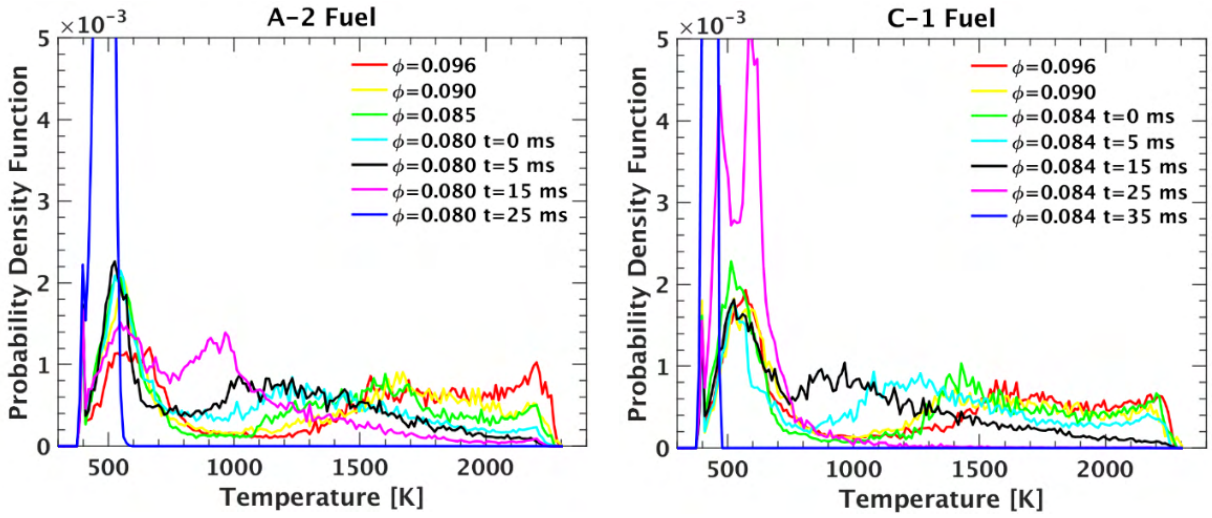

Figure 24. Probability density function of the temperatures of the recirculating gases in the primary zone for A-2 fuel (left) and C-1 fuel (right). Φ = global equivalence ratio.

Statistical analysis was carried out by generating a probability density function (PDF) of the temperature distribution in the recirculation zone, as demonstrated for fuels A-2 and C-1 in Figure 24. The temperature distribution of the recirculation zone shows a nonuniform, multi-modal distribution with a peak in the 500 K zone, and a major part of the distribution spread in the range of 1500 K to 2300 K. This indicates that high temperatures are a major part of the recirculation zone and play a significant role in stabilizing the flame. The reduced fuel flow rates corresponding to the stable operation condition exhibit a similar distribution; however, the distributions show more bias toward the low temperatures. At the blowout equivalence ratio, the distribution was observed to have shifted significantly. The second peak of the bimodal distribution corresponding to the high-temperature region was now at a significantly lower temperature compared with the previous equivalence ratios. As the flame finally approached LBO, we observed that this distribution shifted toward the low temperature region and merged into a delta PDF type of distribution. Thus, it can be seen that, as the flame blows out, the recirculation zone cools due to the decrease in overall heat release rates. This lowers evaporation rates and further triggers a reduction in heat release, leading to a cyclical process. This weakening of the recirculation zone is a key marker of flame stability. A significant shift in the PDF distribution of temperatures of the recirculating fluid can be marker for the start of LBO.

Conclusions

A comprehensive CFD LES methodology using autonomous meshing and AMR was developed for simulating the as-it-is realistic engine combustor and successfully demonstrated for the referee combustor. Flow through all combustor passages, including the tiny effusion holes, was resolved in this approach for accurate estimation of the combustor flow field. Flow rate calculations were performed for component-wise and total flow splits for all passages in the referee combustor. RANS and LES models with different mesh resolutions captured the flow splits correctly. The computational results agreed reasonably well with experimental data of nonreacting flow splits from a complex combustor.

LES successfully captured the fuel sensitivity for A-2 and C-1 fuels on the LBO limits with HyChem skeletal and compact kinetic mechanisms. Predicted LBO trends agreed well with experimental data. Several sensitivity studies were performed to identify best practices: (1) computational domain sensitivity: we analyzed the influence of plenum size on the combustor flow fields; (2) mesh sensitivity; (3) combustion model sensitivity: we evaluated a detailed chemistry solver with laminar FRC and FGM models; (4) chemical kinetic mechanisms sensitivity: HyChem and compact kinetic mechanism model. The model setup consists of a detailed spray injection along with well-defined flow boundary conditions. The modeling approach was initially validated against a stable operating point, where the global equivalence ratio was 0.096. The Lagrangian spray setup was able to capture the trends in spray SMD and velocities for both fuels. Qualitative comparisons of flame shapes were made by comparing line-of-sight averaged OH mass fraction from the computations with OH* from the chemiluminescence.

All kinetic mechanisms predicted similar flame shapes. The overall flame shape and the peak location of the OH were found to be in reasonable agreement with experimental data, providing confidence in the further calculation for LBO computations for both fuels.

The blowout process was studied in detail by analyzing the heat release rate, temperatures, and intermediate species distributions in the primary zone of the referee combustor. The main aim was to identify key markers across different conditions and fuels that could be used to identify stability limits. Two main observations were identified that mark the onset of an unstable flame. We observed in simulations that formation of intermediate species such as formaldehyde moves toward the richer regions of the flame as the LBO limit is approached. These high concentrations indicate incomplete oxidation near the LBO limits. Compared with A-2, C-1 fuel showed significantly higher CH_2O formation in richer regions for the same equivalence ratio and exhibited a higher LBO limit. The temperature in the recirculation zone was also an important indicator of flame stability. The temperature distributions showed a remarkable shift as an unstable configuration is approached. The observation was consistent for both fuels with different LBO limits. Overall, our results support the feasibility of using CFD models to evaluate different fuels and their figures of merit, like LBO, for a realistic gas turbine combustor in a predictive fashion. Further work is needed to understand why CFD models with certain kinetic mechanisms did not produce the correct LBO trends. Future work will involve predicting LBO trends for other alternative fuels, as well as simulating cold-start ignition and high-altitude relight and developing an improved feature sensitivity analyses of LBO's dependence on individual physical and chemical kinetic characteristics. These efforts will help to develop a robust LES CFD methodology for accurate prediction of fuel sensitivity on combustion, operability limits, and emissions. These high-fidelity computational tools can be very helpful in the industry for combustor design evaluations and fuel certification process.

Publications

1. Veeraraghava Raju Hasti, Robert P. Lucht, and Jay P. Gore, "Large eddy simulation of hydrogen piloted CH_4 / air premixed combustion with CO_2 dilution", Journal of the Energy Institute, Volume 93,Issue3,June2020,Pages1099-1109 https://doi.org/10.1016/j.joei.2019.10.004
2. Veeraraghava Raju Hasti, Abhishek Navarkar, and Jay P. Gore , "A data-driven discovery using machine learning for identification of the critical flame location and early detection of the lean blowout in a gas turbine combustor", Energy and AI (Submitted – Under Review)
3. Veeraraghava Raju Hasti, Prithwish Kundu, Sibendu Som, and Jay P. Gore, "Numerical simulations and analysis of the complex turbulent flow field in a realistic gas turbine Combustor", Proceedings of the Institution of Mechanical Engineers, Part A: Journal of Power and Energy (Submitted – Under Review)
4. M.S. Anand, Jeffery A. Lovett, Jeff Moder, Thomas Wey, Matthias Ihme, Lucas Esclapez, Peter C. Ma, Suresh Menon, Achyut Panchal, Veeraraghava Raju Hasti, Jay Gore, Pritwish Kundu, Sibendu Som, Venkat Raman, Yihao Tang, Fang Xu, Vaidya Sankaran, "Chapter IX. CFD Modeling of Lean Blowout and Ignition Fuel Sensitivity", AIAA Book Series (Submitted - Under Review)
5. Veeraraghava Raju Hasti, Prithwish Kundu, Gaurav Kumar, Scott A. Drennan, Sibendu Som, and Jay P. Gore. "A Numerical Study of Flame Characteristics during Lean Blow-Out in a Gas Turbine Combustor", 2018 Joint Propulsion Conference, AIAA Propulsion and Energy Forum, (AIAA 2018-4955)
6. Veeraraghava Raju Hasti, Prithwish Kundu, Gaurav Kumar, Scott A. Drennan, Sibendu Som, Sang Hee Won, Frederick L. Dryer, and Jay P. Gore. "Lean blow-out (LBO)
computations in a gas turbine combustor", 2018 Joint Propulsion Conference, AIAA Propulsion and Energy Forum, (AIAA 2018-4958).
7. Veeraraghava Raju Hasti, Prithwish Kundu, Gaurav Kumar, Scott A. Drennan, Sibendu Som, and Jay P. Gore. "Numerical Simulation of Flow Distribution in a Realistic Gas Turbine Combustor", 2018 Joint Propulsion Conference, AIAA Propulsion and Energy Forum, (AIAA 2018-4956).
8. Veeraraghava Raju Hasti, Gaurav Kumar, Shuaishuai Liu, Robert P. Lucht, and Jay P. Gore. "Large Eddy Simulation of Pilot Stabilized Turbulent Premixed CH4+Air Jet Flames", 2018 AIAA Aerospace Sciences Meeting, AIAA SciTech Forum, Kissimmee, Florida, USA (AIAA 2018-0675)
9. Veeraraghava Raju Hasti, Shuaishuai Liu, Gaurav Kumar, and Jay P. Gore. "Comparison of Premixed Flamelet Generated Manifold Model and Thickened Flame Model for Bluff Body Stabilized Turbulent Premixed Flame", 2018 AIAA Aerospace Sciences Meeting, AIAA SciTech Forum, Kissimmee, Florida, USA (AIAA 2018-0150)